Spin and charge order in the CE phase of $La_{1-x}Ca_xMnO_3$

P. Schlottmann
Department of Physics, Florida State University, Tallahassee, Florida 32306, USA
(Received 2 July 2009; published 24 September 2009)

The CE phase of $La_{1-x}Ca_xMnO_3$ is stable for $x \gtrsim 0.5$ and displays long-range magnetic, charge, and orbital orders. The magnetic order of the Mn spins arises from the competition of the superexchange and double-exchange interactions and the checkerboard charge and the orbital order is the consequence of the Jahn-Teller coupling of the e_g orbitals to the lattice. Using a mean-field slave-boson approach for the e_g electrons in two orbitals per site with excluded multiple occupancy and Hund's rule coupling between the e_g and t_{2g} states, we obtain the tight-binding band structure of the CE phase. The unit cell of the CE phase consists of 16 sites. The 32 e_g bands in the Brillouin zone are grouped into two sets of 16 bands separated by a charge order gap. The phase diagram including the A, B, C, CE, and G phases reproduces the phase sequence observed in $La_{1-x}Ca_xMnO_3$.

DOI: 10.1103/PhysRevB.80.104428 PACS number(s): 75.47.Lx, 75.10.Lp, 71.28.+d

I. INTRODUCTION

The rich phase diagram of $La_{1-x}Ca_xMnO_3$ (LCMO) is the consequence of the interplay of spin, charge, orbital, and lattice degrees of freedom.[1,2] The end compounds of LCMO, $LaMnO_3$ and $CaMnO_3$, are antiferromagnetic (AFM) insulators while for intermediate x the system is either a ferromagnetic (FM) metal or a charge-ordered AFM and may display phase separation.[3–5] In addition, Jahn-Teller distortions, orbital order, and spin canting play an important role. Many of the phases of LCMO were identified in early papers[6,7] and denoted with A, B, C, CE, and G according to their magnetic and charge orders. In the B phase all localized spins are FM correlated while in the G phase each up spin is surrounded by neighbors with down spins and vice versa. In the A phase the localized spins are FM oriented in the x-y planes and these planes are AFM stacked along the z direction. The C phase consists of FM chains along the z direction, which are AFM correlated to each other in the x-y plane. The CE phase is considerably more complex involving 16 sites per unit cell with magnetic, charge, and orbital orders.

In perovskites the range of substitutions, e.g., La by Ca, is limited by the tolerance factor. The tolerance factor is defined as the ratio of the distance between the cation R and O ions and the MnO bond length divided by $\sqrt{2}$, i.e., $d_{R-O}/(\sqrt{2}d_{Mn\text{-}O})$. Only for LCMO the tolerance factor is close to one and the alloy can form over the entire concentration range, $0 \leq x \leq 1$.[6,8]

In a previous publication[9] we studied LCMO as a cubic lattice of mixed-valent Mn ions with the t_{2g} spins (treated classically) oriented in the spin arrangements of the A, B, C, and G phases.[6] The multiple occupancy of the e_g levels at each site is prevented by a large Coulomb interaction, which is taken into account with auxiliary bosons in the mean-field approximation. The e_g electrons are allowed to hop between nearest-neighbor sites with amplitude t, which gives rise to the ferromagnetic double exchange.[10,11] We obtained the band structure for the e_g electrons and the ground-state energy for each of the phases. For a given doping x the phase diagram then only depends on one parameter, namely, J/t. The results improve if the hopping matrix element for the longer FM bonds is rescaled to $t-\delta t$ while AFM links are kept with hopping t.[9] In this paper we extend this calculation to include the more involved CE phase. This way the sequence of phases of LCMO as a function of x is reproduced for J/t on the order of a few percent. The parameter δt plays an important role in the fine tuning of the phase diagram.

Our results[9] have been extended to include the Jahn-Teller coupling to the lattice.[12] A Jahn-Teller distortion lifts the degeneracy of the e_g levels and changes the band structure. Due to the anisotropic spin configurations of the A and C phases the stability of these phases grows at the expense of the B and G phases. The Jahn-Teller distortion consists of a compression (expansion) of the c axis for the A phase (C phase) (Ref. 12) in agreement with experiments.[6,13] Further extensions of this calculation involve instabilities toward the canting of spins and long-range orbital order in the A phase.[14–16]

In this paper we present an extensive study of the CE phase. The CE phase is considerably more complex than the other phases, consisting of 16 sites in two planes per unit cell with magnetic, charge, and orbital orders. Our emphasis here is on the spin arrangements and the checkerboard order of e_g charges. Early models for the CE phase involve FM zigzag chains[1] and Monte Carlo simulations on small system sizes[17,18] and interfaces.[19] Mean-field approaches[20,21] and *ab initio* band-structure calculations[22] were carried out more recently.

The rest of the paper is organized as follows. In Sec. II we restate the basic model for all the manganite phases. In Sec. III the unit cell of the CE phase is introduced as well as the interaction between sites arising from the Jahn-Teller coupling to the lattice which is needed to drive the charge order. In Sec. IV we obtain the band structure for the e_g electrons for $x=0.5$, a self-consistent mean-field solution for the ground state of the CE phase and the J/T vs x phase diagram which is compared to the experimental observations for LCMO. Concluding remarks are presented in Sec. V.

II. MODEL

In LCMO the Mn ions form a nearly simple-cubic lattice with one oxygen ion located approximately on the center of

each side and the trivalent La or divalent Ca atoms at the body center. The O^{2-} ions mediate the binding between the Mn ions while the role of La and Ca doping is to provide conduction electrons.[7] The Mn ions are in a mixed trivalent ($3d^4$) and tetravalent ($3d^3$) state which depends on x. In cubic symmetry the five $3d$ levels are split into a t_{2g} triplet and an e_g doublet. Within octahedral coordination the t_{2g} states have lower energy than the e_g orbitals so that the three t_{2g} orbitals are all singly occupied with their spins coupled to form a total spin $S=3/2$. The e_g orbitals, on the other hand, are empty for Mn^{4+} and occupied by one $3d$ electron in Mn^{3+}, which is FM correlated with the t_{2g} electrons (Hund's rule) to form a total spin $S^*=2$. The intermediate-valence character of the Mn ions arises from the hopping of the e_g electrons.

A. Electronic and magnetic interactions

The Hamiltonian is written as $H=H_t+H_m$, where H_t represents the hopping of the e_g electrons between the Mn sites on a simple-cubic lattice and H_m is the magnetic energy arising from the superexchange between the t_{2g} spins. At this point we neglect the Jahn-Teller coupling of the e_g electrons to the lattice (see below).

The nearest-neighbor hopping Hamiltonian for the e_g electrons is given by[9,23]

$$H_t = -\mu \sum_{jM^*m} |jS^*M^*m\rangle\langle jS^*M^*m| - t \sum_{\langle jl\rangle m_j m_l \sigma M_j M_l M_j^* M_l^*} \left(SM_j, \frac{1}{2}\sigma | S\frac{1}{2} S^* M_j^*\right) \times \left(SM_l, \frac{1}{2}\sigma | S\frac{1}{2} S^* M_l^*\right) \{|jS^*M_j^*m_j\rangle\langle jSM_j| \times \hat{M}_{m_j m_l}(\mathbf{R}_{jl}) |lSM_l\rangle\langle lS^*M_l^*m_l| + \text{H.c.}\}. \quad (1)$$

Here the bra and ket denote the states of the Mn^{4+} configuration represented by a spin $S(=3/2)$ and z-projection M, and the states of the Mn^{3+} configuration of spin $S^*=S+\frac{1}{2}(=2)$ and spin projection M^*. The localized $3d$ electrons are then all FM correlated (first Hund's rule). The Clebsch-Gordan coefficients select the spin components and are needed to preserve the spin rotational invariance. j labels the sites on a simple-cubic lattice. The index $m=x^2-y^2, z^2$ labels the e_g orbitals and σ is the spin component of the e_g electron. The Mn^{3+} states have in addition a label m to indicate which of the e_g states is occupied. The completeness condition for the states requires that at every site

$$\sum_{M^*m} |jS^*M^*m\rangle\langle jS^*M^*m| + \sum_M |jSM\rangle\langle jSM| = 1, \quad (2)$$

which excludes the multiple occupancy of the e_g levels, i.e., they can only be empty or occupied by one electron. This corresponds to an implicit infinite on-site Coulomb repulsion.

The first term in Eq. (1) determines the chemical potential μ for the itinerant electrons while the second term corresponds to the nearest-neighbor intersite hopping. The sum is over all the nearest-neighbor pairs $\langle jl\rangle$ and $\mathbf{R}_{jl}$ is the vector joining the sites j and l. The hopping matrix $\hat{M}_{m_j m_l}(\mathbf{R}_{jl})$ depends on $\mathbf{R}_{jl}$, i.e., $\hat{M}_x=(2\hat{I}+\hat{\tau}_z+\sqrt{3}\hat{\tau}_x)/4$, $\hat{M}_y=(2\hat{I}+\hat{\tau}_z-\sqrt{3}\hat{\tau}_x)/4$, and $\hat{M}_z=(\hat{I}-\hat{\tau}_z)/2$. Here $\hat{I}$ and $\hat{\tau}_i$ are the identity and Pauli matrices for the orbital pseudospin of components (x^2-y^2, z^2). These hopping matrices are determined by the overlap of the asymptotes of the e_g wave functions. The fact that x^2-y^2 and z^2 orbitals on neighboring sites have in general nonzero overlap implies that m is not a good quantum number.

The magnetic energy H_m arises from the superexchange of the t_{2g} spins mediated by the oxygen atoms and depends on the spin configuration of each phase, i.e., A, B, C, CE, and G phases of $La_{1-x}Ca_xMnO_3$.[6] In mean field the Heisenberg superexchange reduces to $H_m=-\alpha JS^2N$, where $\alpha_A=-1$, $\alpha_B=-3$, $\alpha_C=+1$, $\alpha_{CE}=+1$, and $\alpha_G=+3$. Here N is the number of Mn sites. The coupling strength J can be estimated from the transition temperature of the end compounds and should be on the order of 100 times smaller than the hopping t.

B. Slave-boson mean-field approximation

We introduce slave-boson creation and annihilation operators,[9,24] $b_{jM}^\dagger$ and b_{jM}, which act as projectors onto the states of the Mn^{4+} configuration with spin component M at site j, and fermion operators for the Mn^{3+} states at the site j, $d_{jM^*m}^\dagger$, and d_{jM^*m}, with spin and orbital components M^* and m. The completeness relation (2) is now

$$\sum_M b_{jM}^\dagger b_{jM} + \sum_{M^*m} d_{jM^*m}^\dagger d_{jM^*m} = 1. \quad (3)$$

Transitions between configurations are described by the operators $|jSM\rangle\langle jS^*M^*m| = b_{jM}^\dagger d_{jM^*m}$. The total Hamiltonian in the auxiliary space is now given by

$$H = -\alpha JS^2N - \mu \sum_{jM^*m} d_{jM^*m}^\dagger d_{jM^*m} - t \sum_{\langle jl\rangle m_j m_l \sigma M_j M_l M_j^* M_l^*} \left(SM_j, \frac{1}{2}\sigma | S\frac{1}{2} S^* M_j^*\right) \times \left(SM_l, \frac{1}{2}\sigma | S\frac{1}{2} S^* M_l^*\right) \{d_{jM_j^*m_j}^\dagger b_{jM_j} \times \hat{M}_{m_j m_l}(\mathbf{R}_{jl}) b_{lM_l}^\dagger d_{lM_l^*m_l} + \text{H.c.}\}, \quad (4)$$

subject to the constraint [Eq. (3)], which restricts the model to the physical subspace. The above slave-boson formulation is exact, i.e., it does not contain approximations with respect to the original Hamiltonian.

The spin-projections $M_j=\pm S$ of the t_{2g} moments are determined by the magnetic phase under consideration. The spin projection of the Mn^{3+} ion is $M_j^*=\pm S+\sigma$ and hence the spin component σ of the e_g electron is a good quantum number. σ is either parallel or antiparallel to M_j yielding a Clebsch-Gordan coefficient equal to 1 or $1/\sqrt{2S+1}$, respectively. We denote these coefficients $a_{j\sigma}$ and the index M_j^* of the fermion operators can be replaced by σ, i.e., $d_{j\sigma m}$.

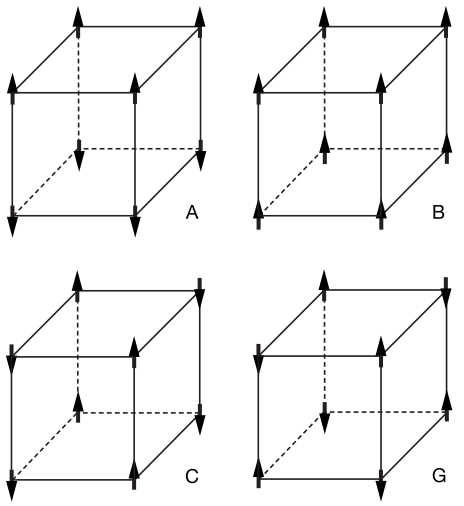

FIG. 1. Magnetic order of the A, B, C, and G phases of LCMO. There are two Mn ions in the unit cell of the A, C, and G phases while the one of the B phase consists of only one Mn atom. Within the present approximations only the relative direction of the spins is important but the ground-state energy is invariant under the simultaneous rotation of all the spins.

Hamiltonian (4) subject to the constraint [Eq. (3)] is studied in the mean-field (saddle-point) approximation,[9] i.e., the boson operators are replaced by their expectation values.[25] Since in the A, B, C, and G phases all Mn sites have the same valence we have $\langle b_{jM_j}\rangle=\langle b^\dagger_{jM_j}\rangle=b$ for $M_j=S$ or $M_j=-S$, depending on the magnetic configuration and all others are zero. The case of the CE phase is discussed in Sec. III. The constraint [Eq. (3)] is incorporated via a Lagrange multiplier $\lambda_j=\lambda$, which is the same for all sites. The mean-field Hamiltonian is

$$H_{mf}=-\alpha JS^2N-N\lambda(1-b^2)+(\lambda-\mu)\sum_{j\sigma m}d^\dagger_{j\sigma m}d_{j\sigma m}-tb^2\sum_{\langle jl\rangle\sigma m_j m_l}a_{j\sigma}a_{l\sigma}\times[d^\dagger_{j\sigma m_j}\hat{M}_{m_j m_l}(\mathbf{R}_{jl})d_{l\sigma m_l}+\text{H.c.}]. \quad (5)$$

All five phases have different magnetic unit cells. The magnetic order of the A, B, C, and G phases is shown in Fig. 1. While the unit cell of the B phase has only one ion, the ones of the A, C, and G phases have two Mn ions and the unit cell of the CE phase has 16 sites.[6] The band structure for the e_g electrons is obtained by Fourier transforming and diagonalizing Eq. (5). For the A, C, and G phases there are four bands arising from the two e_g levels and the two sites per unit cell. In the case of the B phase the four bands arise from the two e_g levels and the spin.[9] The band structure of the CE phase is discussed in Sec. IV. We denote the diagonal states with a tilde, i.e., $\tilde{d}^\dagger_{\mathbf{k}\sigma\alpha}$, where $\alpha=1,\ldots,4$ and the corresponding energies with $E^t_\alpha(\mathbf{k})$. The occupation numbers $\langle\tilde{d}^\dagger_{\mathbf{k}\sigma\alpha}\tilde{d}_{\mathbf{k}\sigma\alpha}\rangle$ are given by Fermi functions. The ground-state energy

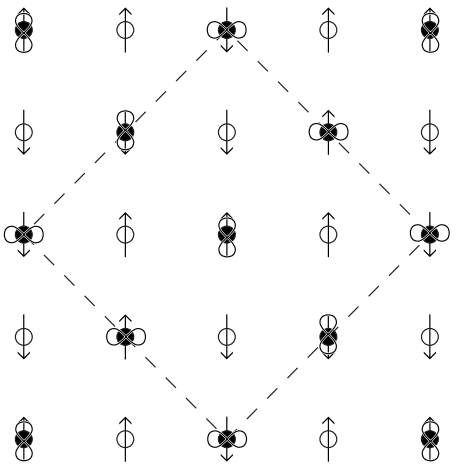

FIG. 2. Checkerboard pattern for the charge order in the CE phase of LCMO. The open (filled) circles correspond to a site with decreased (increased) charge. The arrows indicate the magnetic order in the plane. The spins in successive planes are alternately antiparallel and parallel to this plane with identical charge configuration. The bows indicate the $3x^2-r^2$ and $3y^2-r^2$ orbital order of the nearly trivalent sites. The dashed lines denote the unit cell which altogether contains 16 sites (two planes).

$$E_{GS}=-\alpha JS^2N-N\lambda(1-b^2)+\sum_{\mathbf{k}\alpha}[\lambda-\mu+E^t_\alpha(\mathbf{k})]f[\lambda-\mu+E^t_\alpha(\mathbf{k})] \quad (6)$$

is minimized with respect to b and λ. This yields two transcendental equations, which are solved self-consistently.

III. CE PHASE

The CE phase has a checkerboard charge order in addition to the complex magnetic order in the x-y plane shown in Fig. 2. All spins are reversed in the neighboring planes but the $\vec{Q}$ vector for the charge order is $(\pi,\pi,0)$. The dashed lines in Fig. 2 denote the unit cell in the x-y plane. Note that the up spins form a zigzag chain in the (1,1,0) direction with a unit length of two lattice spacings. Considering the double exchange, this path has the largest hopping amplitude and is the favorite direction for the propagation of the e_g electrons.[1]

The model for the CE phase is $H=H_t+H_m+H_W$, where H_t and H_m are the hopping of the e_g electrons and the superexchange interaction discussed in the previous section. Here H_W is the interaction driving the charge order. The description in terms of auxiliary bosons, Eq. (4), with the completeness condition (3) also remains valid. The mean-field approximation has to be reformulated since the valence is no longer the same at every Mn site. We have to distinguish between two different charge states, i.e., two different boson expectation values, b_1 and b_2. Similarly, the completeness condition requires two different Lagrange parameters for the two sites, λ_1 and λ_2. Although the completeness condition is formally the same at every site, e.g., Eq. (3), a different potential λ is required at the two sites to enforce completeness. The expectation value of the ground-state energy has now to be minimized with respect to b_1, b_2, λ_1, and λ_2.

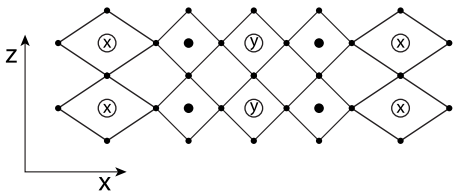

FIG. 3. Checkerboard charge order and antiferro-orbital order of the CE phase as seen in the x-z plane. The dark circles represent the smaller Mn^{4+} ions and the open circles the larger Mn^{3+} ions. The trivalent ions have an e_g electron either in the $3x^2-r^2$ or $3y^2-r^2$ orbital, denoted with x and y, respectively. The straight segments join the O^{2+} ions of the MnO_6 octahedra. The octahedra containing a Mn^{3+} ion are elongated along the axis of the orbital.

Without an interaction H_W driving the charge imbalance there is no charge order, i.e., $b_1=b_2$ and $\lambda_1=\lambda_2$, and the valence is the same at every Mn site. If the charge order would be driven by a nearest-neighbor Coulomb interaction the wave vector for the order would be $\vec{Q}=(\pi,\pi,\pi)$ and not $(\pi,\pi,0)$. The most likely origin of H_W is the Jahn-Teller effect. There are three normal modes of vibration of the MnO_6 octahedra usually denoted by Q_1, Q_2, and Q_3.[26] Here Q_1 corresponds to the breathing mode which preserves the symmetry of the octahedron. Q_2 and Q_3 deform the octahedron preserving its volume. This lifts the degeneracy of the e_g orbitals.

For simplicity we first argue with integer valent Mn ions. Octahedra containing a Mn^{3+} ion occupy a larger volume than those with a Mn^{4+} ion because of the presence of the e_g electron. In addition, the e_g electron is in a specific orbital (or linear combination of orbitals), which in the present notation is either $3x^2-r^2$ or $3y^2-r^2$. The octahedra are elongated along the direction of the axis of the orbital. This gives rise to antiferro-orbital order with alternating $3x^2-r^2$ and $3y^2-r^2$ orbitals on the Mn^{3+} sites, which is the most efficient way to fill the area of the x-y plane by displacing the corner-shared oxygen ions. Along the z direction the orbitals remain the same (see Fig. 3). The geometry of the displacements of the oxygen ions in one x-y plane leads to identical displacements in the nearest-neighbor planes. Consequently, the charge order has $\vec{Q}=(\pi,\pi,0)$ and the e_g electrons in neighboring planes are in the same orbitals. The above arguments do not change if the Mn ions are mixed valent (with partial charge order) instead of integer valent.

The most important contribution to H_W is mediated by the Q_1 mode and we will ignore the other two modes here. The Jahn-Teller Hamiltonian consists of two terms, namely, the elastic deformation energy of the lattice and the coupling of the e_g electrons to the phonons,[26]

$$H_{JT}=\frac{N}{2}\sum_{\mathbf{p}} C(\mathbf{p})\tilde{Q}_1^*(\mathbf{p})\tilde{Q}_1(\mathbf{p}) + 2N\sum_{\mathbf{p}} g(\mathbf{p})\mathrm{Re}\,\tilde{Q}_1(\mathbf{p})\sum_{\sigma m}\rho_{\sigma m}(\mathbf{p}), \tag{7}$$

where $C(\mathbf{p})$ is the phonon energy, $g(\mathbf{p})$ the coupling constant, $\tilde{Q}_1(\mathbf{p})$ is the phonon eigenmode with momentum $\mathbf{p}$, and $\rho_{\sigma m}(\mathbf{p})$ is the charge-density wave with momentum $\mathbf{p}$ of spin σ and orbital m. We keep only the staggered mode with momentum $(\pi,\pi,0)$, which is the relevant one for the charge order. Minimizing H_{JT} with respect to the amplitude $\tilde{Q}_1(\mathbf{p})$ we obtain

$$\tilde{Q}_1(\mathbf{p})=-2\frac{g(\mathbf{p})}{C(\mathbf{p})}(\hat{n}_1-\hat{n}_2),$$

$$H_{JT}=-2N\frac{g(\mathbf{p})^2}{C(\mathbf{p})}(\hat{n}_1-\hat{n}_2)^2, \tag{8}$$

where $\hat{n}_1$ and $\hat{n}_2$ are the average e_g occupation of the sublattices, i.e., $\hat{n}_l=(2/N)\Sigma_{j,\sigma,m}d^\dagger_{j\sigma m}d_{j\sigma m}$ for $l=1,2$ with j belonging to the sublattice l.

This interaction vanishes for $\hat{n}_1=\hat{n}_2$, i.e., the A, B, C, and G phases are not affected by this interaction. The effect of this interaction is maximum in the CE phase for $x=0.5$. Denoting $W=8[g(\mathbf{p})]^2/C(\mathbf{p})$, the mean-field Hamiltonian H_W is

$$H_W=(W/2)(b_1^2-b_2^2)\sum_{j,\sigma,m}(-1)^{l+1}d^\dagger_{j\sigma m}d_{j\sigma m}, \tag{9}$$

where $l=1$ or 2 depending on whether j belongs to the sublattice 1 or 2, leading to a staggered potential.

The interaction strength W is x dependent. If $x>1/2$ there are more e_g holes than required for half filling. This allows the e_g electrons to move more freely and as a consequence the lattice softens, i.e., the elastic constant $C(\mathbf{p})$ is reduced. Similarly, the coupling of the e_g electrons to the lattice, $g(\mathbf{p})$, is expected to increase with the mobility of the electrons. Hence, $W(x)$ is an increasing function for $x>1/2$. The contrary occurs for $x<1/2$. Now there are more e_g electrons than needed for half filling and the hard-core repulsion makes their motion more difficult. The elastic energy increases and the electron-phonon coupling weakens due to the defects in the checkerboard superstructure. Due to the hard core there is clearly an asymmetry between $x>1/2$ and $x<1/2$. Assuming that $W(x)$ is an analytic function of x at $x=1/2$, we expand

$$W(x)=W_0[1+\alpha(x-1/2)+\cdots], \tag{10}$$

where α is a dimensionless constant of the order of unity. We only keep the linear term in $(x-1/2)$ and neglect higher order contributions.

The e_g bands are obtained by Fourier transforming and diagonalizing the mean-field Hamiltonian using the spin configuration of the CE phase. The e_g band structure for $x=0.5$ has been presented in Ref. 27. In Sec. IV we calculate the total energy, which is then minimized with respect to b_1, b_2, λ_1, and λ_2. This yields transcendental equations, which are solved self-consistently.

In models (1) and (4) the complicated nature of the Mn-O bonds is strongly simplified. Experimentally it has been found that FM nearest-neighbor bonds are considerably longer than those of AFM bonds.[6] This is most likely due to Jahn-Teller distortions of MnO_6 octahedra.[12] The actual lattice parameters strongly depend on the sample preparation.[13] In Ref. 9 we incorporated the change in the hopping t and the superexchange J due to deviations from the cubic symmetry.

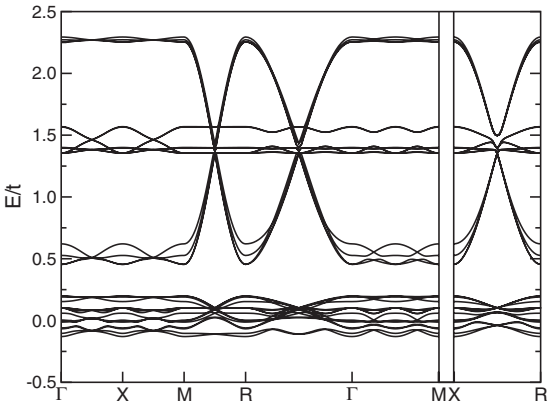

FIG. 4. Band structure for electrons in the e_g orbitals of the CE phase at $x=0.5$. The parameters are $W=3.11t$, $\delta t/t=0.1$, $n_1=0.900$, $n_2=0.100$, $\lambda_1=1.3914t$, and $\lambda_2=0.1554t$. The Fermi level is at zero energy. The charge order gap separates the 32 bands into two subgroups of 16 bands.

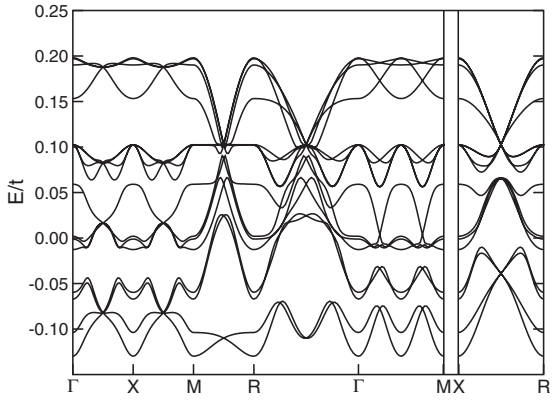

FIG. 5. Expanded view of the 16 lower energy e_g bands of the CE phase at $x=0.5$. The parameters are the same as in Fig. 4. The Fermi energy is at zero energy. A strong collective Jahn-Teller effect involving the Q_2 and Q_3 modes would open a gap at the Fermi level and render an insulating orbitally ordered ground state.

The simplest approach is to assume that the hopping decreases with the distance between the Mn sites, i.e., that it is reduced by the amount δt for a FM bond as compared to an AFM bond.[9] Hence, we denote with t the hopping matrix element of an electron between AFM correlated sites and with $t-\delta t$ the hopping between sites with parallel spins. This effect is assumed to be due to the change in bond length only and is additional to the Clebsch-Gordan coefficients that favor hopping if the spins are all parallel (double exchange). We will choose $\delta t/t=0.1$. The superexchange involves the fourth power of the charge transfer between a Mn ion and O^{2-}, i.e., it is quadratic in t. Hence, the reduction in J, i.e., $\delta J/J$, is just given by $2\delta t/t$. The effect of δt on the band structure of the A, B, C, and G phases and the J/t vs x phase diagram for these four phases has been discussed in Ref. 9. In the following section we limit ourselves to analyze the consequences for the CE phase.

IV. RESULTS

A. Band structure of e_g electrons in the CE phase

We adopt the simple-cubic Brillouin zone to facilitate a comparison with the other phases already discussed in Ref. 9. The Γ point corresponds to $\mathbf{k}=0$ at the body center of the cube, the X point at the center of the face, the M point at the middle of a side, and the R point at the corner of the cubic Brillouin zone. Due to the magnetic order, the x, y, and z directions are not equivalent. The band structure shown is along the following directions: from Γ to X along $\mathbf{k}=(k_x,0,0)$, then from X to M varying k_y from 0 to π along $(\pi,k_y,0)$, from M to R along (π,π,k_z), from R to Γ along $(k/\sqrt{3})(1,1,1)$, and from Γ to M along $(k/\sqrt{2})(1,1,0)$. Finally, X to R refers to the line $(\pi,k/\sqrt{2},k/\sqrt{2})$.

The CE phase has 32 bands arising from the two e_g orbitals of the 16 sites of the unit cell. Figure 4 displays the 32 e_g bands separated by the charge order gap into two subsets of 16 bands each. The Fermi level is at zero energy. Note that the upper bands are much broader than the lower energy subset. This is the consequence of the hard-core potential which allows each site to be occupied by at most one e_g electron (completeness condition). The charge gap then plays no role neither for the ground-state nor the low-energy excitations.

The bands within each group of 16 bands are further grouped into four sets of four bands (see Fig. 5). A strong Jahn-Teller effect involving a staggered mode of $3x^2-r^2$ and $3y^2-r^2$ orbitals (linear combination of the two e_g orbitals) would open a gap separating the four lowest bands from the remaining bands. Only under these circumstances is the system an insulator, in agreement with the experimental findings. The insulating state is then not a consequence of the charge gap. The parameter δt does not play an important role in this context.

B. Self-consistent solution

The numerical solution of the transcendental equations determining b_1, b_2, λ_1, and λ_2 depends on x, W, and to a lesser extent on δt. $b_1=b_2$ and $\lambda_1=\lambda_2$ is always a solution, although not necessarily the one with lowest energy. However, not every value of W leads to a solution with charge imbalance, $b_1\neq b_2$. This is seen in Fig. 6, where W/t is displayed as a function of $(n_1-n_2)/(n_1+n_2)$ for various values x. For $x=0.5$ the range of W for which there are solutions is rather narrow. This range is expected to increase if the interaction mediated by the collective Q_2 and Q_3 modes is also included (orbital order). Note the asymmetry of the curves as a function of x about half filling.

The ground-state energy for the hopping Hamiltonian (excluding the energy of the superexchange $\langle H_m\rangle$) is shown in Fig. 7 as a function of the relative charge imbalance $(n_1-n_2)/(n_1+n_2)$ between the two sublattices for $\delta t=0.1t$. For the larger values of x (fewer e_g electrons than half filling) the energy is independent of the charge imbalance while for $x<1/2$ (more e_g electrons than half filling) the energy becomes strongly dependent on $(n_1-n_2)/(n_1+n_2)$.

C. Phase diagram

The phase diagram is constructed by comparing the ground-state energies of the five phases for a given x and J/t.

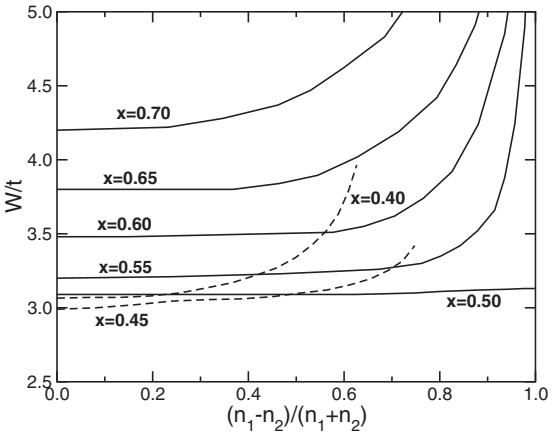

FIG. 6. W/t vs the relative charge imbalance $(n_1-n_2)/(n_1+n_2)$ between the two sublattices obtained from the self-consistent solution of the transcendental equations for $\delta t=0.1t$ for various x. For $x=1/2$ the solutions correspond to a narrow interval of W while for $x\neq 1/2$ the range is much larger. The curves for $x<1/2$ are shown as dashed lines.

For the A, B, C, and G phases the ground-state energy (for fixed x) when normalized to the hopping t is only a function of J/t. The ground-state energy of the CE phase depends, in addition, on the interaction parameters W_0 and α [see Eq. (10)]. We chose $W_0=3.11t$ and $\alpha=1.6$.

Several energy crossovers are obtained for fixed x and as a function of the superexchange coupling J. The phase diagram is shown in Fig. 8. For sufficiently large J the G phase is always the stable one since it has all AFM bonds and hence the lowest magnetic energy. The B phase with all FM correlated bonds has the lowest energy at most values of x for small J. Here the double exchange is the dominating magnetic interaction. The FM correlations are rapidly quenched by the AFM superexchange J. The A, C, and CE phases are intermediate phases between the FM B phase and the AFM G phase. The CE phase involves a staggered charge order and is therefore only stable close to half filling. The calculation for the phases other than the CE phase is identical to that reported in Fig. 5(b) in Ref. 9.

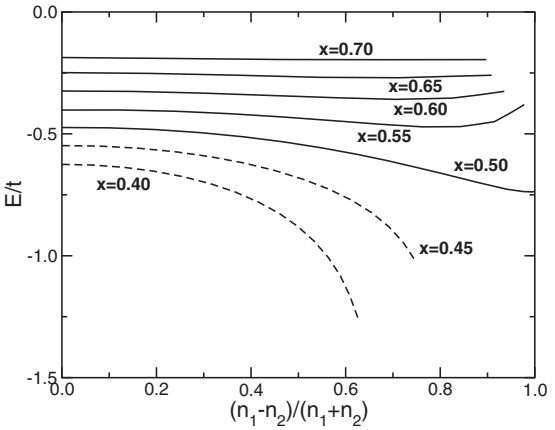

FIG. 7. Ground-state energy as a function of the relative charge imbalance $(n_1-n_2)/(n_1+n_2)$ between the two sublattices for the same parameters as in Fig. 6. Note the qualitative change in the energy dependence for the various values of x.

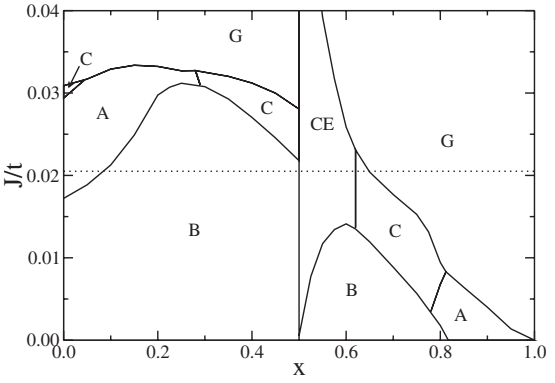

FIG. 8. Phase diagram obtained by comparing the ground-state energies of the five phases as a function of J/t and x for the distorted lattice for which the FM correlated bonds have a hopping matrix element reduced by a factor $(1-\delta t/t)$. Here $\delta t=0.1t$ and for the CE phase we have chosen $W_0=3.11t$ and $\alpha=1.6$. The dotted line corresponds to the sequence of phases observed for LCMO (Ref. 6).

In comparison to the other phases the CE phase is clearly most stable for half filling. The remarkable asymmetry of the CE phase about the line $x=1/2$ is in part due to the asymmetric behavior observed in Figs. 6 and 7, and in part a consequence of the x dependence of W. Due to the hard-core repulsion among the e_g electrons (i.e., the assumption that the only allowed configurations are Mn^{3+} and Mn^{4+}) it is not the same to have checkerboard charge order with more than half filling than with less than half filling. The CE phase with charge order abruptly disappears for $x<1/2$. The value of α is not critical for the phase diagram. A smaller value for α only slightly reduces the range of stability of the CE phase.

In Fig. 9 the effect of δt on the phase diagram is shown. The global picture remains unchanged, although δt weakens the B phase as compared to the G phase. For small x the A phase becomes stable for lower values of J/t while the range of stability of the C phase is reduced. The dotted horizontal line in Fig. 8 roughly reproduces the sequence of phases (A-B-CE-C-G) found for LCMO as a function of x. The main importance of the parameter δt is to improve the agreement with the experiment. A detailed comparison with experiments is difficult in view of phase separation in the vi-

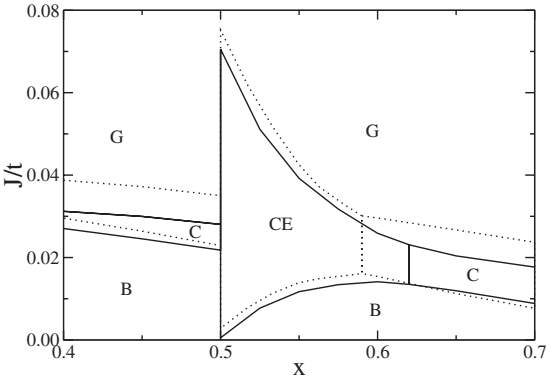

FIG. 9. Comparison of the phase diagram for $\delta t=0.1t$ (solid lines) with that for $\delta t=0$ (dashed curves). The parameters for the CE phase are $W_0=3.11t$ and $\alpha=1.6$.

cinity the phase boundaries. Here phase B is the only phase with a spontaneous magnetization.

V. CONCLUDING REMARKS

We considered a simple-cubic lattice of intermediate valent Mn ions, with three localized $3d$ electrons in the t_{2g} orbitals and itinerant e_g electrons. The density of e_g electrons is determined by the degree of doping, i.e., $1-x$. The first of Hund's rules couples all the $3d$ electrons ferromagnetically, maximizing the total spin at each Mn site. The t_{2g} spins of the Mn ions interact with each other via a nearest-neighbor superexchange mediated by the oxygen $2p$ electrons. In LCMO the low-temperature phases are all magnetically ordered. The e_g electrons can hop between nearest-neighbor sites with hopping amplitudes that depend on the orbital (x^2-y^2 or $3z^2-r^2$) and the magnetic phase. The excluded multiple occupancy of the e_g levels at each Mn site (due to large Coulomb interactions) limits the Mn to be between trivalent and tetravalent (intermediate valent) and is taken into account via slave bosons in the saddle-point approximation.

In this paper we focused on the CE phase, which displays charge order and orbital order in addition to the magnetic order. The unit cell for this phase consists of 16 sites. Due to the charge imbalance, two slave-boson expectation values have to be introduced, one for each sublattice. The driving force inducing the charge order is predominantly mediated by the Jahn-Teller coupling to the breathing Q_1 mode of the MnO_6 octahedra, although the Q_2 and Q_3 vibration modes also may play an important role, in particular, concerning the long-range orbital order of the CE phase. The deviations from cubic symmetry of the lattice affect the hopping t and the superexchange J. FM correlated bond lengths are slightly longer than AFM correlated links. We took this effect into account by reducing by δt the hopping matrix element of a FM bond and similarly reducing the exchange by δJ.

For the driving potential for the charge order we only considered the Q_1 Jahn-Teller mode, neglecting the coupling to the Q_2 and Q_3 modes. The Q_1 mode (volume of the octahedra) yields the dominant contribution to charge order. A consequence of this approximation is that for $x=0.5$ a self-consistent solution only exists over a very narrow range of W_0/t values. This essentially determines the value of W_0/t within the present scheme. We believe that if the interactions mediated by the Q_2 and Q_3 modes are included, the range of W_0/t for which solutions are available would be considerably larger. The value of the parameter α is less critical; it does not affect the physics close to $x=0.5$ and only determines the range of the stability of the CE phase for larger x. The larger the value of α, the larger is the range of stability of the CE phase.

We calculated the band structure of the CE phase, which consists of 32 e_g bands separated by the charge order gap into two subsets of 16 bands each. Due to the excluded multiple occupancy of the e_g levels at every Mn site (hard-core potential) the charge gap does not directly affect the ground-state and the low-energy excitations of the CE phase. A strong collective Jahn-Teller coupling to the Q_2 and Q_3 modes is needed to generate the staggered orbital order involving $3x^2-r^2$ and $3x^2-r^2$ orbitals. For $x=1/2$ the long-range orbital order opens a gap at the Fermi level rendering an insulating CE phase, in agreement with experimental observations. The CE phase is energetically very favorable for half filling; for departures from half-filling phase separation into a half-filled CE phase and a B phase ($x<1/2$) or C phase ($x>1/2$) is then to be expected.

The self-consistent solution of the mean-field equations shows a strong anisotropy about half filling. This is again the consequence of the hard-core potential. We found that the CE phase is favored in a small region for $x \gtrsim 1/2$. For $x<1/2$ the stable phase is the FM B phase and for larger x the C phase has lower energy. The inclusion of the parameter δt is important to reproduce the experimental sequence of phases for LCMO.[6]

ACKNOWLEDGMENT

The support by the U.S. Department of Energy under Grant No. DE-FG02-98ER45707 is acknowledged.

[1] E. Dagotto, T. Hotta, and A. Moreo, Phys. Rep. **344**, 1 (2001).
[2] M. B. Salamon and M. Jaime, Rev. Mod. Phys. **73**, 583 (2001).
[3] S. Yunoki, J. Hu, A. L. Malvezzi, A. Moreo, N. Furukawa, and E. Dagotto, Phys. Rev. Lett. **80**, 845 (1998); A. Moreo, S. Yunoki, and E. Dagotto, Science **283**, 2034 (1999).
[4] L. P. Gor'kov and V. Z. Kresin, J. Supercond. **12**, 243 (1999).
[5] P. Schlottmann, Phys. Rev. B **59**, 11484 (1999).
[6] E. O. Wollan and W. C. Koehler, Phys. Rev. **100**, 545 (1955).
[7] J. Goodenough, Phys. Rev. **100**, 564 (1955).
[8] R. von Helmolt, J. Wecker, B. Holzapfel, L. Schultz, and K. Samwer, Phys. Rev. Lett. **71**, 2331 (1993); K. Chahara, T. Ohuo, M. Kasai, and Y. Kozono, Appl. Phys. Lett. **63**, 1990 (1993); G. C. Xiong, Q. Li, H. L. Ju, S. N. Mao, L. Senapathi, X. X. Xi, R. L. Greene, and T. Venkatesan, *ibid.* **66**, 1427 (1995); Y. Tokura, A. Urishibara, Y. Moritomo, T. Arima, A. Asamitsu, G. Kido, and N. Furukawa, J. Phys. Soc. Jpn. **63**, 3931 (1994).
[9] P. Schlottmann, Phys. Rev. B **62**, 439 (2000).
[10] C. Zener, Phys. Rev. **82**, 403 (1951); P. W. Anderson and H. Hasegawa, *ibid.* **100**, 675 (1955).
[11] A. J. Millis, P. B. Littlewood, and B. I. Shraiman, Phys. Rev. Lett. **74**, 5144 (1995); N. Furukawa, J. Phys. Soc. Jpn. **64**, 2734 (1995).
[12] P. Schlottmann, Phys. Rev. B **73**, 214428 (2006).
[13] Q. Huang, A. Santoro, J. W. Lynn, R. W. Erwin, J. A. Borchers, J. L. Peng, K. Ghosh, and R. L. Greene, Phys. Rev. B **58**, 2684 (1998).
[14] P. Schlottmann, IEEE Trans. Magn. **43**, 3085 (2007).
[15] P. Schlottmann, Physica B **384**, 187 (2006).
[16] P. Schlottmann, Physica B **403**, 1642 (2008).

[17] T. Hotta, A. L. Malvezzi, and E. Dagotto, Phys. Rev. B **62**, 9432 (2000).
[18] H. Aliaga, D. Magnoux, A. Moreo, D. Poilblanc, S. Yunoki, and E. Dagotto, Phys. Rev. B **68**, 104405 (2003).
[19] S. Dong, R. Yu, S. Yunoki, J. M. Liu, and E. Dagotto, Phys. Rev. B **78**, 064414 (2008).
[20] S. M. Dunaevsky and V. V. Deriglazov, Phys. Rev. B **75**, 214408 (2007).
[21] S. Dong, S. Dai, X. Y. Yao, K. F. Wang, C. Zhu, and J.-M. Liu, Phys. Rev. B **73**, 104404 (2006).
[22] R. Bastardis, C. de Graaf, and N. Guihéry, Phys. Rev. B **77**, 054426 (2008).
[23] P. Schlottmann, Phys. Rev. B **60**, 7911 (1999).
[24] S. E. Barnes, J. Phys. F: Met. Phys. **6**, 1375 (1976); P. Coleman, Phys. Rev. B **29**, 3035 (1984).
[25] N. Read and D. M. Newns, J. Phys. C **16**, L1055 (1983).
[26] J. Kanamori, J. Appl. Phys. **31**, S14 (1960).
[27] P. Schlottmann, J. Phys.: Conf. Ser. **150**, 042176 (2009).